

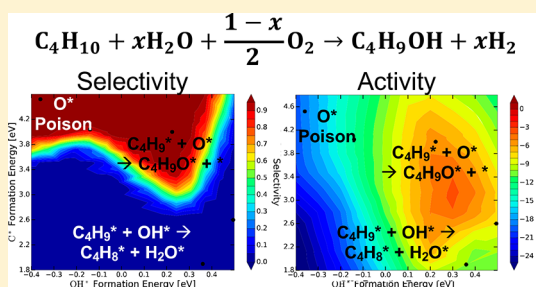
# Reaction Pathways and Microkinetic Modeling of *n*-Butane Oxidation to 1-Butanol on Cu, Cu<sub>3</sub>Pd, Pd, Ag<sub>3</sub>Pd, and PdZn (111) Surfaces

Jiazhou Zhu and Rachel B. Getman\*

Department of Chemical and Biomolecular Engineering, Clemson University, Clemson, South Carolina 29634-0909, United States

## Supporting Information

**ABSTRACT:** Density functional theory (DFT) calculations and microkinetic modeling are used to model reactions in the oxidation of *n*-butane to 1-butanol, 1-butanal, and 1-butene over pure metal and metal alloy (111) surfaces. Specifically, catalytic thermodynamic and kinetic energies are calculated with DFT, and linear scaling relationships are developed that link these values to simpler “descriptors” of catalytic activity. The scaling relationships are used in microkinetic modeling to identify the optimal descriptor values, which maximize the rate and selectivity to 1-butanol. Degree of rate control (DRC) analysis is performed to reveal the catalytic intermediates and transition states that have the greatest influence on the rate. The Cu<sub>3</sub>Pd(111) and Ag<sub>3</sub>Pd(111) surfaces are found to be the most active for *n*-butane oxidation to 1-butanol, with Cu<sub>3</sub>Pd additionally exhibiting high selectivity for 1-butanol. Achieving high activity and selectivity toward 1-butanol is found to require a precise balance of the catalyst affinity for OH\* and O\*, with catalysts that bind these species too strongly garnering large coverages of O\*, which block active sites and inhibit the rate of *n*-butane conversion, and catalysts that bind these species too weakly promoting dehydrogenation of C<sub>4</sub> species, as this process supplies H atoms that can convert OH\* and O\* to the more-stable H<sub>2</sub>O\*. Catalytic affinity for C\* is also found to have a significant impact on selectivity toward 1-butanol, since the formation energy of C\* on catalyst surfaces is found to correlate to catalytic ability to break C–H bonds, with catalysts that bind C\* too strongly tending to overdehydrogenate C<sub>4</sub> species. The reaction C<sub>4</sub>H<sub>9</sub>\* + O\* ↔ C<sub>4</sub>H<sub>9</sub>O\* + \* is found to be rate-controlling on those catalysts that are most active for 1-butanol production.



## 1. INTRODUCTION

Designing catalysts to selectively convert reactants to desired products is a grand challenge, especially when undesired products are energetically more favorable.<sup>1,2</sup> Alkane oxidations to alcohols are key examples of reactions where selectivity is challenging. One important reaction in this class is *n*-butane oxidation to 1-butanol. From a practical standpoint, 1-butanol is used as a solvent, coating, cleaner, and furnishing product.<sup>3–6</sup> From a research perspective, it provides an interesting problem in selectivity, since other products of oxidation, including 2-butanol, 1-butanal, and of course CO<sub>2</sub>, are more thermodynamically stable.<sup>7</sup>

One way to control selectivity is to use a catalyst that is capable of promoting reactions in the pathway to the alcohol and preventing reactions in the pathways to all other possible products.<sup>1,8</sup> To produce 1-butanol from *n*-butane, a catalyst that targets the primary carbon must be employed. NP@MOF catalysts have shown promise in this regard.<sup>9,11</sup> NP@MOF catalysts are comprised of metal nanoparticle (NP) catalysts encapsulated by metal organic frameworks (MOFs),<sup>10</sup> which are permanently porous, crystalline materials comprised of metal or metal oxide nodes connected by organic “linker” molecules.<sup>12</sup> Hypothetically, if a MOF with a sufficient, one-dimensional (1D) pore structure could be used to encapsulate a metal catalyst capable of selectively converting alkanes to alcohols, then that

catalyst could be used to target the primary carbon of *n*-butane. Indeed, our experimental collaborators have previously demonstrated that the NP@MOF catalyst Pt@ZIF-8 can target the primary carbon of linear alkenes for catalytic hydrogenation, specifically hydrogenating trans-1,3-hexadiene to 3-hexene with high selectivity.<sup>9</sup> Thus, it seems possible that the steric constraints supplied by the ZIF-8 encapsulation are capable of restricting catalytic activation to the terminal carbon of a linear hydrocarbon. Motivated by the possibility of such regioselective catalysts, our goal in this work is to identify design parameters for the NP component of the catalyst that control activity and selectivity toward a terminal alcohol.

Looking into the literature, the challenge of selectively oxidizing alkanes to alcohols is clear. For one, adsorbed O atoms (i.e., O\*), e.g., formed via O<sub>2</sub> dissociation, have been shown to promote C–H bond activation.<sup>15–19,22</sup> If the desired reaction is oxidation of the alkane to an alcohol, this can inhibit selectivity by promoting activation of more than just the desired C–H bond,<sup>13,14</sup> even for sterically constrained catalysts.<sup>16</sup> This is particularly challenging, given that some form of surface oxygen

Received: February 5, 2018

Revised: March 29, 2018

Accepted: April 9, 2018

Published: April 9, 2018

is needed to promote alkane oxidation to alcohols. Selectivity toward the desired alcohol thus requires that the surface be highly active toward C–O and O–H bond formation and/or that the reaction conditions are tuned to very precisely control the surface coverage of O\*.<sup>16</sup> In terms of transition-metal surfaces, Cu and PdZn have been shown to exhibit energetics that could favor selectivity toward oxidation instead of dehydrogenation,<sup>20,21</sup> however, these metals have very high affinities for O\*, which could limit their effectiveness in practice. Because of the challenge of achieving high activity and high selectivity, in practice, researchers have turned to novel catalysts<sup>23–25,27,28</sup> and/or more aggressive oxidants, e.g., N<sub>2</sub>O and O<sub>3</sub>.<sup>25,26,29</sup> Ideally, however, it is preferable to utilize a catalyst that could be employed in large scale industrially, along with O<sub>2</sub> or another abundant oxidant (e.g., H<sub>2</sub>O).

In order to learn the features of transition-metal NP catalysts that promote activity and selectivity for alkane selective oxidations, in this work, we use a combination of density functional theory (DFT) and microkinetic modeling to calculate the thermodynamics and kinetics of reactions likely to be involved in the dominant reaction pathway for *n*-butane oxidation to 1-butanol, using molecular oxygen and water as oxidants.<sup>30</sup> We explicitly calculate these values on Cu(111), Cu<sub>3</sub>Pd(111), Pd(111), Ag<sub>3</sub>Pd(111), and PdZn(111) surfaces. We then evaluate descriptors of catalytic activity and construct linear scaling relationships that can be used to write catalytic thermodynamic and kinetic values as continuous functions of the descriptor values. These are then input to microkinetic modeling, which is used to determine optimal descriptor values and reaction conditions that optimize activity and selectivity to 1-butanol.

All of our simulations are performed over sterically constrained transition-metal surfaces. Following protocols established in our prior work,<sup>16</sup> steric constraints are included with “surrogate pore” models,<sup>31</sup> which are cylinders comprised of He atoms that are stacked above the catalyst surfaces. These surrogate pore models simply prevent the reaction intermediates from “laying down” on the catalyst surfaces,<sup>31</sup> thus serving as models for catalysts that can restrict activity to the terminal carbons of linear hydrocarbons. Since these models do not take the chemical interplay between the catalyst encapsulation (e.g., the MOF) and the NP into account, the exact metal compositions that we study in this work may not directly translate to compositions that would be used in practice. However, the general conclusions that we make about reaction mechanisms, catalytic descriptors, relative surface coverages, and optimal operating conditions should be widely useful in the quest to design active and selective catalysts for alkane oxidation to alcohols.

## 2. COMPUTATIONAL METHODS

**2.1. Encapsulated Catalyst Surface Models.** Cu(111), Cu<sub>3</sub>Pd(111), Pd(111), Ag<sub>3</sub>Pd(111), and PdZn(111) catalysts are modeled by cutting three-layer 5 metal atom × 5 metal atom (Cu), three-layer 4 metal atom × 4 metal atom (Cu<sub>3</sub>Pd and PdZn), or four-layer 4 metal atom × 4 metal atom (Pd, Ag<sub>3</sub>Pd) periodic surface slabs from the calculated bulk structures of these metals. Pd and Ag<sub>3</sub>Pd were simulated using four-layer slabs in order to best utilize results and calculations from our prior work,<sup>16,31</sup> and the remaining catalysts were modeled as three-layer slabs for better computational tractability. We find a maximum 0.05 eV difference in the formation energies of C\* and OH\*, which are the catalytic descriptors identified in this work,

on the three-layer slabs versus the four-layer slabs. The lateral dimensions for all metals were chosen as the smallest possible that would accommodate the surrogate pores used to model steric constraints (described below). The bulk structures of these metals are as follows. Cu and Pd are fcc metals with calculated (experimentally observed) lattice parameters of 3.50 Å (3.57 Å<sup>32</sup>) and 3.83 Å (3.89 Å<sup>33</sup>), respectively. Cu<sub>3</sub>Pd and Ag<sub>3</sub>Pd are modeled in the L1<sub>2</sub> structure and have calculated lattice parameters of 3.87 and 4.10 Å, respectively. The structure of PdZn is L1<sub>0</sub> with a calculated lattice parameter of 4.15 Å. The Cu<sub>3</sub>Pd(111) slab model is shown in Figure 1 as an example.

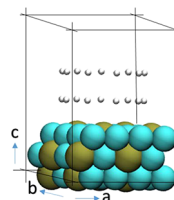


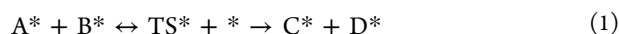
**Figure 1.** Periodic 4 metal atom × 4 metal atom sterically constrained Cu<sub>3</sub>Pd(111) surface slab used to calculate catalytic energetics in this work. Steric constraints are provided by surrogate pores. [Color key: Cu = cyan, Pd = gold, He = white.]

In the periodic surface slabs, 13.5 Å of vacuum space is left between surfaces in the vertical dimension. Atoms in the top two layers of the metal slabs are allowed to relax, while the remaining atoms are held fixed in their calculated bulk positions. Steric constraints are provided by the surrogate pore model.<sup>31</sup> As in our prior work,<sup>16,30</sup> surrogate pores are comprised of discrete He atoms, which provide steric constraints without affecting the energies of catalytic surface intermediates or transition states. The surrogate pores are cylinders with diameters of 8.8 Å and heights of 2.8 Å, and they are placed 3.5 Å above the metal atoms in the topmost layers of the surface slabs. Reaction intermediate- and transition-state structures are also placed on the topmost layers of the metal surface slabs. The total surface coverage, which is defined as the number of reaction intermediates or transition states per surface metal atom, is equal to 1/25 (Cu monolayer (ML), where 1 ML is equal to 1 adsorbate per surface metal atom) or 1/16 ML (Cu<sub>3</sub>Pd(111), Pd(111), Ag<sub>3</sub>Pd(111), and PdZn(111)), i.e., meaning that there is just one reaction intermediate or transition state per slab in all of the calculations presented in this manuscript.

**2.2. Density Functional Theory Calculations.** Density functional theory (DFT) calculations are performed with the VASP code,<sup>34,35</sup> which is a periodic boundary condition code that uses planewave basis sets. Electron exchange and correlation are calculated using the Perdew–Burke–Ernzerhof (PBE) functional,<sup>36</sup> and energies of core electrons are simulated with PAW pseudopotentials<sup>35,37</sup> to an energy cutoff of 400 eV. The D2 method of Grimme<sup>38</sup> is employed to improve the modeling of dispersion interactions in all calculations. Gamma-centered *k*-point meshes of 7 × 7 × 1 are used to sample the first Brillouin zones. Supercell calculations are performed non-spin-polarized. Ionic relaxations are carried out until the magnitudes of all of the forces on all of the nonfixed atoms are less than 0.03 eV/Å. A combination of the climbing image nudged elastic band (CI-NEB)<sup>39,40</sup> and dimer methods<sup>41</sup> is used to locate the transition states. Vibrational modes are calculated to verify that the calculated transition states are first-order saddle points in the directions of the reaction coordinates. All other details about the

sterically constrained surface models and DFT calculations are identical to those reported in ref 16.

**2.3. Calculation of Reaction Energies and Activation Barriers.** Reaction energies and activation barriers are calculated according to the following reaction:



where  $TS^*$  is the transition-state complex, the asterisk symbol (\*) denotes an empty site on the metal catalyst surface, and species with an asterisk are bound to the catalyst slab models. From this reaction,

$$E_{\text{rxn}} = E_{C^*} + E_{D^*} - E_{A^*} - E_{B^*} \quad (2)$$

and

$$E_{\text{act}} = E_{TS^*} + E_* - E_{A^*} - E_{B^*} \quad (3)$$

where  $E^*$  is the energy of the clean surface.

**2.4. Descriptor Identification and Microkinetic Modeling.** Identification of catalytic descriptors, construction of scaling relationships, and microkinetic modeling are performed with the CatMAP software,<sup>42</sup> and the interested reader can find our CatMAP input file in section S3 in the Supporting Information. Briefly, catalytic descriptors are energies of adsorbates that are well-correlated to the energies of all the relevant catalytic intermediates and transition states in a reaction network, and scaling relationships are the functions that relate the energies of the reaction intermediates and transition states to the catalytic descriptors.<sup>29</sup> (Specifically, descriptors are formation energies of adsorbates that are well-correlated to the formation energies of all the relevant catalytic intermediates and transition states in a reaction network. The conversion between formation energy and electronic energy is provided in eqs S1–S4 in the Supporting Information). We construct scaling relationships as linear functions of two descriptors in this work. Descriptors are chosen so that the mean absolute error (MAE) between the energies predicted by the scaling relationships and the values calculated with DFT are minimized. This procedure is elaborated more fully in our prior work.<sup>43</sup> In this work, we find that the energies of the reaction intermediates  $C^*$  and  $OH^*$  give the lowest MAE, and thus they are used as descriptors. The descriptor combinations that we tested along with their MAEs are provided in Table S6.1 in the Supporting Information. Scaling relationships for all the catalytic intermediates and transition states considered in this work are provided in Figures S8.1–S8.27 in the Supporting Information. We find that a relevant transition state in the production of 1-butanol from *n*-butane is for the reaction  $C_4H_9^* + O^* \leftrightarrow C_4H_9O^* + *$  (i.e., rxn r8, shown later in this work), and that a relevant surface intermediate is  $O^*$ . The scaling relationships for these species are presented in Figure 2 as examples.

Microkinetic modeling is performed at 423 K and 3750 kPa  $C_4H_{10}(g)$ , 456 kPa  $H_2O(g)$ , either 2 kPa or  $1 \times 10^{-8}$  kPa  $O_2(g)$ , and trace amounts of  $C_4H_9OH(g)$ ,  $C_4H_8O(g)$ ,  $C_4H_8(g)$ , and  $H_2(g)$ . Specifically, the pressures of  $C_4H_9OH(g)$ ,  $C_4H_8O(g)$ , and  $C_4H_8(g)$  are  $10^{-46}$ ,  $10^{-9}$ , and  $10^{-6}$  kPa, respectively, which represents a total conversion of *n*-butane of  $2.67 \times 10^{-10}$ . These conditions were chosen because they maximize selectivity to 1-butanol. For example, increasing the partial pressure of 1-butanol, relative to 1-butanol, decreases the rate of 1-butanol production in our models. The pressures of  $C_4H_{10}(g)$  and  $H_2O(g)$  that are employed are the saturation pressures of those compounds at 423 K. These conditions were chosen because, in previous work, we showed that they resulted in high selectivity toward 1-

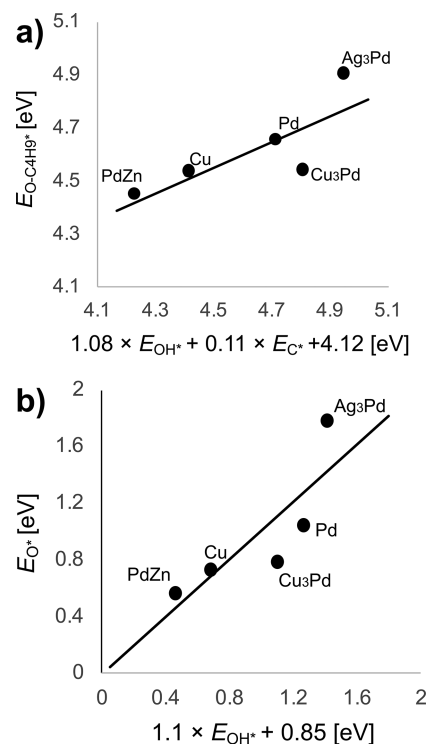


**Figure 2.** Scaling relationships for (a) the transition state for rxn r8 (shown later in this work), i.e.,  $C_4H_9^* + O^* \leftrightarrow C_4H_9O^* + *$ , and (b)  $O^*$ .  $E$  are formation energies, and solid lines are parity lines. [1 eV = 96.485 kJ/mol.]

butanol.<sup>30</sup> In our microkinetic models, all catalytic intermediates are treated using the pseudo-steady-state approximation, and the system is assumed to have reached steady state when the change in the surface coverages of all catalytic reaction intermediates is less than  $10^{-50}$  ML. All gas-phase species are held at constant pressure. We introduce one “dummy” reaction into our microkinetic model,  $C(g) + * \leftrightarrow C^*$ , so that the energy of  $C^*$  can be evaluated by the CatMAP software as a catalytic descriptor, since calculating this value is computationally tractable (and also because it is often used as a descriptor in microkinetic modeling of catalytic reactions involving hydrocarbons<sup>44,45</sup>). However, since our mechanism does not include  $C^*$ , the pressure of  $C(g)$  is set to 0 in our microkinetic models.

**2.5. Analysis of the Microkinetic Modeling Results.** The most rate-inhibiting catalytic intermediates and rate-controlling transition states are identified using the degree of rate control (DRC) method,<sup>46–48</sup> as employed in CatMAP. Briefly,

$$X_{ij} = \left( \frac{d \log(r_i)}{d \left( -\frac{G_j}{kT} \right)} \right)_{G_{n \neq j}} \quad (4)$$

where  $X$  is the DRC matrix,  $r_i$  the rate of desorption of product  $i$ ,  $G_j$  the free energy of species  $j$ ,  $k$  the Boltzmann constant, and  $T$  the temperature. DRC values are calculated numerically by making small changes to the free energy for each reaction intermediate and transition state individually, while holding the free energies of all other species constant. The microkinetic model is then resolved and the results are numerically differentiated. When a catalytic species exhibits a positive DRC value, it means that if that species’ free energy were decreased (i.e., made more negative),  $r_i$  would increase. Conversely, when a

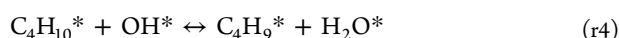
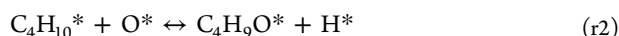
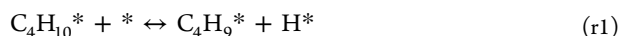


catalytic species exhibits a negative DRC value, it means that if the species' free energy were increased (i.e., made more positive),  $r_i$  would increase. Transition states with positive DRC values are said to be rate-controlling, i.e., a decrease in their free energies would lower a relevant activation barrier and, thus, increase the rate, while catalytic intermediates with negative DRC values are said to be rate-inhibiting, i.e., an increase in their free energies would lead to a lower coverage of these species, which would leave open more free sites for carrying out catalytic reactions.

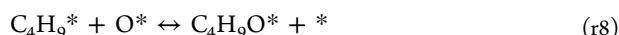
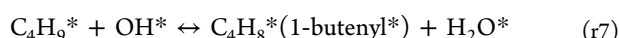
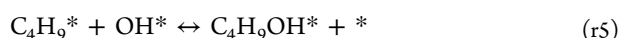
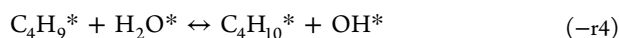
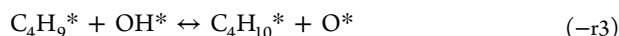
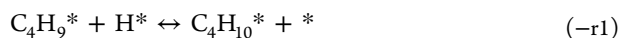
### 3. RESULTS

**3.1. Calculated Reaction Energies and Activation Barriers.** The reactions considered in this work were inspired by our prior manuscript, which used microkinetic modeling to identify the dominant reaction pathway in *n*-butane oxidation to 1-butanol over sterically constrained Ag<sub>3</sub>Pd(111),<sup>30</sup> as well as from the literature on simulations of catalytic alkane oxidation.<sup>17,49–51</sup> They are as follows:

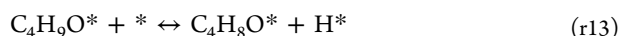
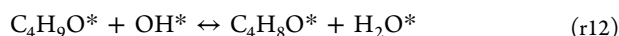
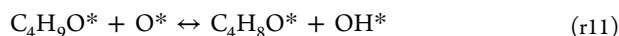
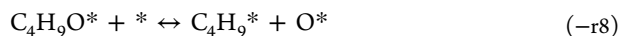
Activation of the first C–H bond:



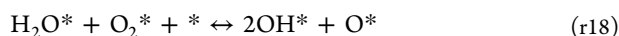
Reactions of  $\text{C}_4\text{H}_9^*$  (i.e., 1-butyl):



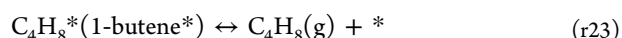
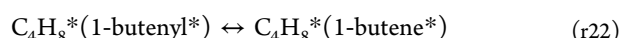
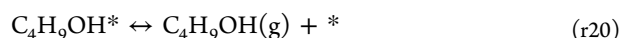
Reactions of  $\text{C}_4\text{H}_9\text{O}^*$  (i.e., 1-butoxy):



Reactions involving  $\text{O}^*$  and  $\text{OH}^*$ :



Other adsorption and desorption reactions:



We note that *rxns* r4, r6, r7, r8, r12, r13, r18, r22, and r23 were not considered in our prior work on Ag<sub>3</sub>Pd(111). The reactions presented above involve activation of a C–H bond on *n*-butane, via direct (*rxn* r1), O\*-assisted (*rxns* r2 and r3), or OH\*-assisted (*rxn* r4) pathways. The  $\text{C}_4$  intermediates that are formed are either 1-butyl ( $\text{C}_4\text{H}_9^*$ ) or 1-butoxy ( $\text{C}_4\text{H}_9\text{O}^*$ ). If 1-butyl is formed, it can react to form 1-butanol ( $\text{C}_4\text{H}_9\text{OH}^*$ , *rxn* r5) or 1-butoxy ( $\text{C}_4\text{H}_9\text{O}^*$ , *rxn* r9), or it can go through an overdehydrogenation step where a second C–H bond is activated to form 1-butenyl (*rxns* r6 and r7); otherwise, it can reverse back to *n*-butane ( $\text{C}_4\text{H}_{10}^*$ ) via the reverse of *rxn* r1, r3, or r4. Taking 1-butoxy as a starting intermediate, it can react to form 1-butanol (*rxns* r9 and r10), or it can go through an overdehydrogenation step to form 1-butanal ( $\text{C}_4\text{H}_8\text{O}^*$ , *rxns* r11, r12, and r13).

Calculated reaction energies and activation barriers for *rxns* r1–r13 on the Cu(111), Cu<sub>3</sub>Pd(111), Pd(111), Ag<sub>3</sub>Pd(111), and PdZn(111) surfaces are provided in Table S5.1 in the Supporting Information. Reaction energies and activation barriers for *rxns* r15, r17, r18, and r24 are provided in Table S5.2 in the Supporting Information. The remaining reactions are assumed to be unactivated, and their reaction energies are reported in Table S5.2. Of these, all except *rxn* r22 are adsorption/desorption reactions. Reaction r22 involves the transfer of a H atom from the secondary carbon on 1-butenyl ( $^*\text{CH}-\text{CH}_2-\text{CH}_2-\text{CH}_3$ ) to its terminal carbon, forming 1-butene ( $^*\text{CH}_2=\text{CH}-\text{CH}_2-\text{CH}_3$ ). We assume that this step, which is not directly mediated by the catalyst surface, is unactivated because the hydrogen transfer fills an unsaturated bond on the terminal carbon of the  $\text{C}_4$  species. A test calculation performed on the Pd surface, which has the most positive energy of reaction for *rxn* r22, supports this assumption, with calculated energies of  $E_{\text{rxn}} = 1.3$  eV and  $E_{\text{act}} = 1.1$  eV. Geometric and structural details for all the reaction intermediates and transition states used to compute these energies are provided in Sections S1 and S2 in the Supporting Information.

**3.1.1. Cu Surface.** From Table S5.1, all the first C–H bond activation steps (1–4) are either thermoneutral or endothermic with relatively high activation barriers on Cu(111); however, reactions involving production of  $\text{C}_4\text{H}_9^*$  have lower activation barriers than the reaction involving the production of  $\text{C}_4\text{H}_9\text{O}^*$ . If  $\text{C}_4\text{H}_9^*$  is formed, the energetics to react with  $\text{H}^*$  (reverse of *rxn* r1),  $\text{OH}^*$  (reverse of *rxn* r3), or  $\text{H}_2\text{O}^*$  (reverse of *rxn* r4) to produce *n*-butane are more favorable than the energetics to produce 1-butanol or 1-butoxy.

**3.1.2. Cu<sub>3</sub>Pd Surface.** Similar to Cu, all steps for activating the first C–H bond on Cu<sub>3</sub>Pd surface have positive reaction energies, and the production of  $\text{C}_4\text{H}_9^*$  is more energetically preferable than the production of  $\text{C}_4\text{H}_9\text{O}^*$ . If formed, the reaction of  $\text{C}_4\text{H}_9^*$  with  $\text{H}^*$  to form  $\text{C}_4\text{H}_{10}^*$  through the reverse of *rxn* r1 is the most energetically preferred step, with  $E_{\text{rxn}} = -0.66$  eV and  $E_{\text{act}} = 0.25$  eV; however, the energetics for the production of 1-butanol and 1-butoxy are more favorable than on

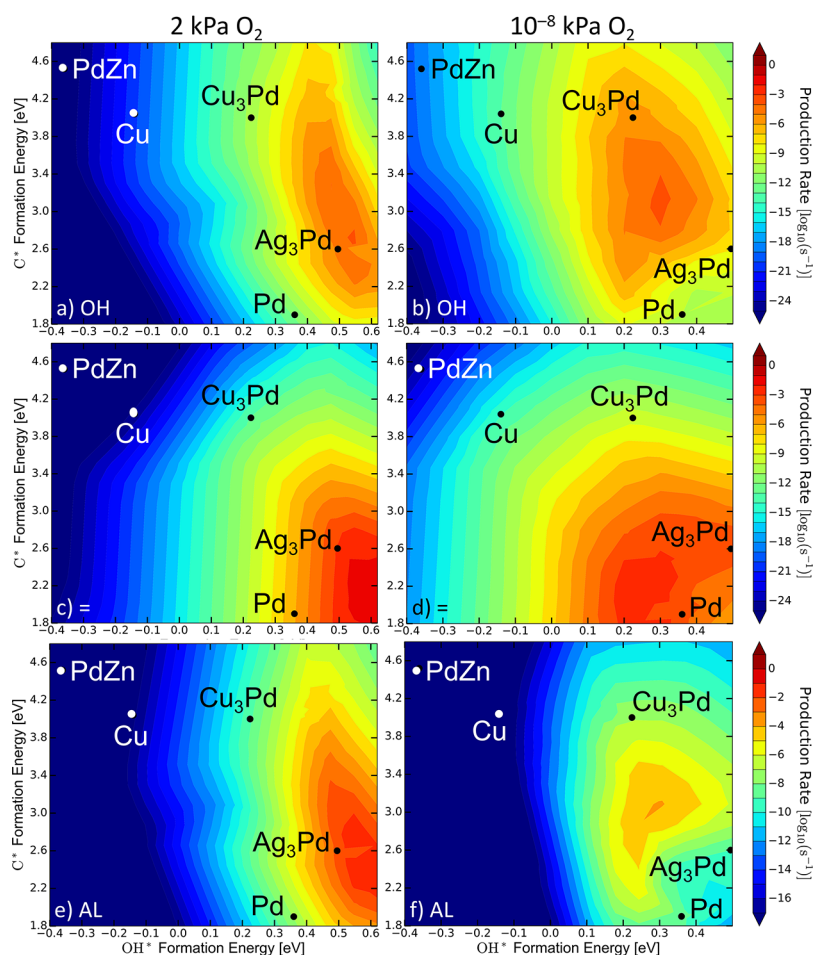


**Figure 3.** Heat maps showing the logarithm of the calculated rates (in units of molecules per site per second) of 1-butanol (OH, top), 1-butene (=, center), and 1-butanol (AL, bottom) desorption as continuous functions of the descriptors at 423 K, 3750 kPa  $C_4H_{10}(g)$ , 456 kPa  $H_2O(g)$ , and 2 kPa  $O_2(g)$  (left-hand side, LHS) or  $10^{-8}$  kPa  $O_2(g)$  (right-hand side, RHS). [1 eV = 96.485 kJ/mol.]

Cu, with **rxn r5**, i.e.,  $C_4H_9^* + OH^* \rightarrow C_4H_9OH^* + *$ , exhibiting  $E_{rxn} = -0.36$  eV and  $E_{act} = 1.53$  eV, and **rxn r8**, i.e.,  $C_4H_9^* + O^* \leftrightarrow C_4H_9O^* + *$ , exhibiting  $E_{rxn} = -0.13$  eV and  $E_{act} = 1.23$  eV. If  $C_4H_9O^*$  forms in this way, the energetics to  $C_4H_9OH^*$  via **rxn r9** ( $E_{rxn} = -0.56$  eV and  $E_{act} = 0.55$  eV) and **rxn r10** ( $E_{rxn} = -0.24$  eV and  $E_{act} = 0.18$  eV) are favorable.

**3.1.3. Pd Surface.** The energetics for activation of the first C–H bond are significantly more favorable on Pd than on Cu and  $Cu_3Pd$ , with **rxns r1–r4** being exothermic, and **rxns r1, r3, and r4** having activation barriers of <1 eV. Particularly, **rxn r1**, i.e.,  $C_4H_{10}^* + * \rightarrow C_4H_9^* + H^*$ , has  $E_{rxn} = -0.29$  eV and  $E_{act} = 0.29$  eV, and **rxn r4**, i.e.,  $C_4H_{10}^* + OH^* \rightarrow C_4H_9^* + H_2O^*$ , has  $E_{rxn} = -0.51$  eV and  $E_{act} = 0.68$  eV, suggesting that *n*-butane activation will proceed through  $C_4H_9^*$ . If  $C_4H_9^*$  is formed, the most energetically favorable route is to  $C_4H_8^*$  via **rxn r7**, i.e.,  $C_4H_9^* + OH^* \leftrightarrow C_4H_8^* + H_2O^*$ , which exhibits  $E_{rxn} = -0.08$  eV and  $E_{act} = 1.09$  eV.

**3.1.4.  $Ag_3Pd$  Surface.** Similar to Pd, activation of the first C–H bond on  $Ag_3Pd$  is facile, with **rxns r2–r4** being exothermic, and **rxns r3 and r4** having barriers of <1 eV. Again, reactions that produce  $C_4H_9^*$  are more energetically favorable than reactions that produce  $C_4H_9O^*$ . If formed, reactions of  $C_4H_9^*$  with  $H^*$  to form *n*-butane (reverse of **rxn r1**,  $E_{rxn} = -0.68$  eV and  $E_{act} = 0.09$  eV),  $O^*$  to form 1-butoxy (via **rxn r8**,  $E_{rxn} = -1.03$  eV and  $E_{act} = 0.62$  eV), and  $O^*$  or  $OH^*$  to form 1-butenyl (**rxns r6 and r7**,  $E_{rxn} = 0.20$  and  $0.52$  eV and  $E_{act} = 0.92$  and  $0.71$  eV, respectively) are

possible. If 1-butoxy is formed, the most energetically preferred route is to 1-butanol via **rxn r11**, i.e.,  $C_4H_9O^* + O^* \leftrightarrow C_4H_8O^* + OH^*$ , which exhibits  $E_{rxn} = -0.92$  eV and  $E_{act} = 0.17$  eV.

**3.1.5.  $PdZn$  Surface.** The most energetically preferred C–H bond activation step on  $PdZn$  is **rxn r3**, i.e.,  $C_4H_{10}^* + O^* \rightarrow C_4H_9^* + OH^*$ , which has  $E_{rxn} = 0.02$  eV and  $E_{act} = 0.73$  eV. If formed, the most energetically preferred route for the  $C_4H_9^*$  intermediate is reaction with  $H^*$  to form *n*-butane through the reverse of **rxn r1**, i.e.,  $C_4H_9^* + H^* \rightarrow C_4H_{10}^* + *$ , with  $E_{rxn} = -0.39$  eV and  $E_{act} = 0.50$  eV.

**3.2. Microkinetic Modeling.** **3.2.1. Production Rates and Optimal Descriptor Values.** Calculated production rates from microkinetic modeling are shown in Figure 3. Figures 3a and 3b plot the logarithm of the rate of desorption of 1-butanol as a continuous function of the descriptors (i.e., the formation energies of  $C^*$  and  $OH^*$ ), calculated at 423 K, 3750 kPa  $C_4H_{10}(g)$ , 456 kPa  $H_2O(g)$ , and 2 kPa  $O_2(g)$  (Figure 3a) or  $1 \times 10^{-8}$  kPa  $O_2(g)$  (Figure 3b). From Figure 3a,  $Ag_3Pd$  is the most active for 1-butanol production at the higher  $O_2$  pressure, and activity follows the trend  $Ag_3Pd > Cu_3Pd > Pd > Cu > PdZn$ . To maximize activity toward 1-butanol, the optimal catalyst would exhibit descriptors of 0.54 eV (formation energy of  $OH^*$ ) and 2.9 eV (formation energy of  $C^*$ ) under these conditions. From Figure 3b,  $Cu_3Pd$  is the most active catalyst at the lower  $O_2$  pressure, and activity follows the trend  $Cu_3Pd > Ag_3Pd > Pd > Cu > PdZn$ . To maximize activity toward 1-butanol, the optimal

**Table 1. Formation Energies in eV (1 eV = 96.485 kJ/mol) That Would Optimize the Production Rates of 1-Butanol, 1-Butene, and 1-Butene at 423 K, 3750 kPa  $C_4H_{10}(g)$ , 456 kPa  $H_2O(g)$ , and  $O_2(g)$  Pressures as Listed**

	Formation Energy (eV)			
	2 kPa $O_2(g)$		$10^{-8}$ kPa $O_2(g)$	
	OH*	C*	OH*	C*
1-butanol	0.54	2.9	0.31	3.1
1-butene	0.60	2.2	0.25	2.2
1-butene	0.58	2.4	0.30	2.9

catalyst would exhibit descriptors of 0.31 eV (formation energy of OH\*) and 3.1 eV (formation energy of C\*) under these conditions. For reference, the activation barrier for rxn r8, i.e.,  $C_4H_9^* + O^* \leftrightarrow C_4H_9O^* + ^*$ , which is a significant step in the pathway to 1-butanol (see section 4.2), is  $\sim 0.9$  eV at these descriptor values. On the  $Cu_3Pd$ , Pd, and  $Ag_3Pd$  surfaces, the difference between the two sets of operating conditions is the coverage: at 2 kPa  $O_2$ ,  $O^*$  is the most abundant surface intermediate on all five metals with coverage approaching 1 ML, whereas at  $10^{-8}$  kPa  $O_2$ , the coverage of  $O^*$  is  $\sim 0.50$  ML on  $Cu_3Pd$ , and there is only trace coverage of  $O^*$  on Pd and  $Ag_3Pd$ . On Cu and PdZn, the coverage of  $O^*$  is  $\sim 1$  ML at both sets of conditions. For reference, the formation energies of  $O^*$  at the volcano peaks for 1-butanol at the higher and lower  $O_2$  pressures, i.e., the darkest orange regions in Figures 3a and 3b, are  $\sim 1.7$  eV and  $\sim 1.5$  eV, respectively. At the lower  $O_2$  pressure of  $10^{-8}$  kPa,  $C_4$  species dominate the surface coverage on Pd and  $Ag_3Pd$ , with coverages approaching 1 ML. (We note that the coverages as quantified here are solutions to the microkinetic models. They

are not equivalent to the coverages that would be observed experimentally, since we have not included coverage effects in the reaction energies and activation energies that were input to the microkinetic models.)

Heat maps showing the production rates of 1-butene and 1-butanol are given in Figures 3c–f. At the higher  $O_2$  pressure, the rate of 1-butene production is maximized at descriptor values of 0.60 eV (formation energy of OH\*) and 2.2 eV (formation energy of C\*), and the rate of 1-butanol production is maximized at descriptor values of 0.58 eV (formation energy of OH\*) and 2.4 eV (formation energy of C\*). At the lower  $O_2$  pressure, the rate of 1-butene production is maximized at descriptor values of 0.25 eV (formation energy of OH\*) and 2.2 eV (formation energy of C\*), and the rate of 1-butanol production is maximized at descriptor values of 0.30 eV (formation energy of OH\*) and 2.9 eV (formation energy of C\*). Optimal descriptor values are summarized in Table 1.

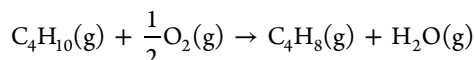
**3.2.2. Overall Reactions.** Under both sets of conditions listed above,  $Cu_3Pd$  and  $Ag_3Pd$  are the most active catalysts that we studied, and thus we focus on these metals for the remainder of the manuscript. The calculated rates of 1-butanol production are  $2.88 \times 10^{-11}$  and  $0.00165$   $s^{-1}$  on these catalysts, respectively, at the higher  $O_2$  pressure, and they are  $4.71 \times 10^{-6}$  and  $1.29 \times 10^{-8}$   $s^{-1}$ , respectively, at the lower  $O_2$  pressure. To understand the mechanism of *n*-butane oxidation to 1-butanol, the net rates of the 24 reactions calculated in microkinetic modeling are presented in Table 2.

Examining the calculated rates of adsorption and desorption, six overall reactions are occurring:

**Table 2. Calculated Net Rates of Reactions r1 through r24 at 423 K, 3750 kPa  $C_4H_{10}(g)$ , 456 kPa  $H_2O(g)$ , and  $O_2(g)$  Pressures as Indicated**

reaction		Net Rate of Reaction (mol site <sup>-1</sup> s <sup>-1</sup> )			
		2 kPa $O_2(g)$		$10^{-8}$ kPa $O_2(g)$	
		$Cu_3Pd$	$Ag_3Pd$	$Cu_3Pd$	$Ag_3Pd$
rxn r1	$C_4H_{10}^* + ^* \leftrightarrow C_4H_9^* + H^*$	$2.97 \times 10^{-14}$	$-0.000102$	$8.95 \times 10^{-6}$	$0.000428$
rxn r2	$C_4H_{10}^* + O^* \leftrightarrow C_4H_9O^* + H^*$	$1.98 \times 10^{-19}$	$5.57 \times 10^{-13}$	$2.24 \times 10^{-15}$	$4.90 \times 10^{-16}$
rxn r3	$C_4H_{10}^* + O^* \leftrightarrow C_4H_9^* + OH^*$	$2.86 \times 10^{-11}$	$0.00171$	$-7.31 \times 10^{-7}$	$-8.99 \times 10^{-6}$
rxn r4	$C_4H_{10}^* + OH^* \leftrightarrow C_4H_9^* + H_2O^*$	$3.75 \times 10^{-13}$	$4.12 \times 10^{-5}$	$-3.49 \times 10^{-6}$	$-0.000205$
rxn r5	$C_4H_9^* + OH^* \leftrightarrow C_4H_9OH^* + ^*$	$2.16 \times 10^{-17}$	$4.24 \times 10^{-9}$	$1.28 \times 10^{-9}$	$1.28 \times 10^{-8}$
rxn r6	$C_4H_9^* + O^* \leftrightarrow C_4H_8^* + OH^*$	$8.75 \times 10^{-19}$	$2.03 \times 10^{-5}$	$8.50 \times 10^{-18}$	$3.57 \times 10^{-9}$
rxn r7	$C_4H_9^* + OH^* \leftrightarrow C_4H_8^* + H_2O^*$	$1.18 \times 10^{-13}$	$0.00138$	$4.15 \times 10^{-10}$	$0.000213$
rxn r8	$C_4H_9^* + O^* \leftrightarrow C_4H_9O^* + ^*$	$2.88 \times 10^{-11}$	$0.000249$	$4.72 \times 10^{-6}$	$7.89 \times 10^{-7}$
rxn r9	$C_4H_9O^* + H^* \leftrightarrow C_4H_9OH^* + ^*$	$2.70 \times 10^{-25}$	$1.33 \times 10^{-15}$	$7.17 \times 10^{-18}$	$2.51 \times 10^{-8}$
rxn r10	$C_4H_9O^* + OH^* \leftrightarrow C_4H_9OH^* + O^*$	$2.88 \times 10^{-11}$	$1.89 \times 10^{-5}$	$4.71 \times 10^{-6}$	$1.43 \times 10^{-10}$
rxn r11	$C_4H_9O^* + O^* \leftrightarrow C_4H_8O^* + OH^*$	$6.26 \times 10^{-14}$	$0.000120$	$2.82 \times 10^{-11}$	$9.64 \times 10^{-13}$
rxn r12	$C_4H_9O^* + OH^* \leftrightarrow C_4H_8O^* + H_2O^*$	$4.01 \times 10^{-20}$	$1.87 \times 10^{-9}$	$6.56 \times 10^{-15}$	$1.42 \times 10^{-14}$
rxn r13	$C_4H_8O^* + ^* \leftrightarrow C_4H_8O^* + H^*$	$2.89 \times 10^{-16}$	$0.000110$	$1.71 \times 10^{-8}$	$7.89 \times 10^{-7}$
rxn r14	$O_2(g) + ^* \leftrightarrow 2O^*$	$1.45 \times 10^{-11}$	$0.000938$	$1.31 \times 10^{-7}$	$3.71 \times 10^{-9}$
rxn r15	$O_2^* + ^* \leftrightarrow 2O^*$	$1.40 \times 10^{-11}$	$0.000938$	$1.04 \times 10^{-10}$	$3.71 \times 10^{-9}$
rxn r16	$H_2O^* \leftrightarrow H_2O(g) + ^*$	$1.66 \times 10^{-13}$	$0.00163$	$-4.46 \times 10^{-6}$	$-7.94 \times 10^{-7}$
rxn r17	$H_2O^* + O^* \leftrightarrow 2OH^*$	$-1.29 \times 10^{-13}$	$-0.000205$	$8.45 \times 10^{-7}$	$8.21 \times 10^{-6}$
rxn r18	$H_2O^* + O_2^* + ^* \leftrightarrow 2OH^* + O^*$	$4.57 \times 10^{-13}$	$1.28 \times 10^{-8}$	$1.31 \times 10^{-7}$	$1.42 \times 10^{-12}$
rxn r19	$C_4H_{10}(g) + ^* \leftrightarrow C_4H_{10}^*$	$2.90 \times 10^{-11}$	$0.00165$	$4.73 \times 10^{-6}$	$0.000214$
rxn r20	$C_4H_9OH^* \leftrightarrow C_4H_9OH(g) + ^*$	$2.88 \times 10^{-11}$	$1.89 \times 10^{-5}$	$4.71 \times 10^{-6}$	$1.29 \times 10^{-8}$
rxn r21	$C_4H_8O^* \leftrightarrow C_4H_8O(g) + ^*$	$6.28 \times 10^{-14}$	$0.000230$	$1.72 \times 10^{-8}$	$7.89 \times 10^{-7}$
rxn r22	$C_4H_8^*(1\text{-butenyl}^*) \leftrightarrow C_4H_8^*(1\text{-butene}^*)$	$1.18 \times 10^{-13}$	$0.00140$	$4.15 \times 10^{-10}$	$0.000213$
rxn r23	$C_4H_8^*(1\text{-butene}^*) \leftrightarrow C_4H_8(g) + ^*$	$1.18 \times 10^{-13}$	$0.00140$	$4.15 \times 10^{-10}$	$0.000213$
rxn r24	$2H^* \leftrightarrow H_2(g) + 2^*$	$1.50 \times 10^{-14}$	$3.98 \times 10^{-6}$	$4.48 \times 10^{-6}$	$0.000214$

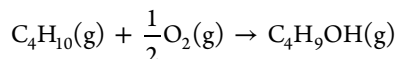
Overall rxn 1:



Overall rxn 2:



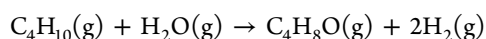
Overall rxn 3:



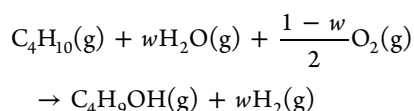
Overall rxn 4:



Overall rxn 5:



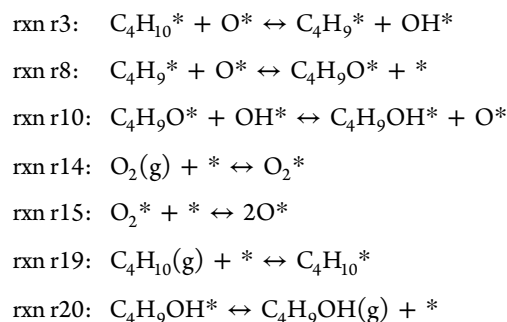
Overall rxn 6:



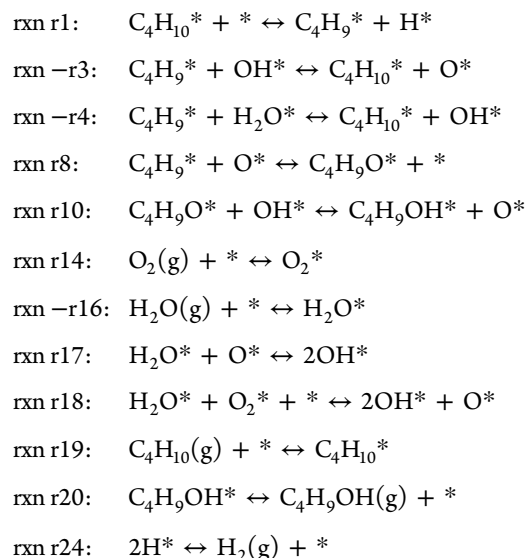
where  $x$ ,  $y$ ,  $z$ , and  $w$  are stoichiometric coefficients that are dependent on the specific catalyst. Overall reactions 1, 2, and 3 occur at the higher  $\text{O}_2$  pressure, while overall reactions 4, 5, and 6 occur at the lower  $\text{O}_2$  pressure. The difference between the overall reactions at the higher versus the lower pressure is the oxidant:  $\text{O}_2$  is the oxidant at the higher  $\text{O}_2$  pressure, while  $\text{H}_2\text{O}$  is a product; however, at the lower  $\text{O}_2$  pressure, there either is no oxidant (overall reaction 4),  $\text{H}_2\text{O}$  is the oxidant (overall reaction 5), or  $\text{H}_2\text{O}$  and  $\text{O}_2$  both act as oxidants (overall reaction 6). This finding is consistent with our prior results on  $\text{Ag}_3\text{Pd}$ ,<sup>30</sup> where  $\text{O}_2$  and  $\text{H}_2\text{O}$  served as oxidants in *n*-butane oxidation to 1-butanol. Examining the rates on  $\text{Ag}_3\text{Pd}$ , at the higher  $\text{O}_2$  pressure, 85% of the *n*-butane that reacts is converted via overall reaction 1, 14% is converted via overall reaction 2, and 1% is converted via overall reaction 3. In contrast, >99% of the *n*-butane that reacts on  $\text{Cu}_3\text{Pd}$  is converted via overall reaction 3. At the lower  $\text{O}_2$  pressure, >99% of the *n*-butane that reacts goes through overall reaction 4 on  $\text{Ag}_3\text{Pd}$ , while on  $\text{Cu}_3\text{Pd}$ , over 99% of the *n*-butane that reacts is converted via overall reaction 6. Thus,  $\text{Cu}_3\text{Pd}$  is selective for 1-butanol, whereas  $\text{Ag}_3\text{Pd}$  is selective for 1-butene and, to some extent, 1-butanal.

**3.2.3. Dominant Reaction Pathways.** The dominant reaction pathways can also be deduced from the results in Table 2, and they are given as follows:

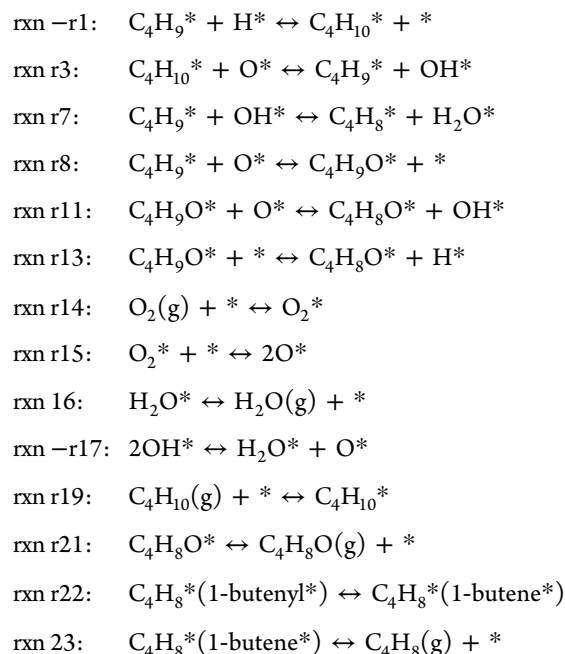
$\text{Cu}_3\text{Pd}$  at 2 kPa  $\text{O}_2(\text{g})$ :



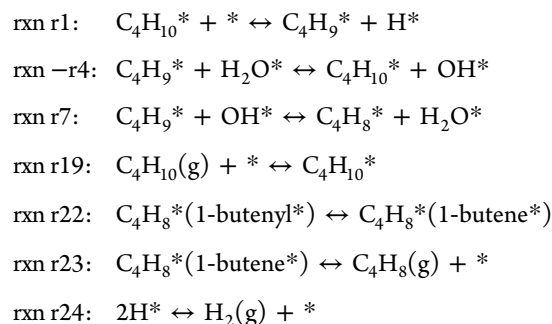
$\text{Cu}_3\text{Pd}$  at  $10^{-8}$  kPa  $\text{O}_2(\text{g})$ :



$\text{Ag}_3\text{Pd}$  at 2 kPa  $\text{O}_2(\text{g})$ :



$\text{Ag}_3\text{Pd}$  at  $10^{-8}$  kPa  $\text{O}_2(\text{g})$ :



At the higher  $\text{O}_2$  pressure on  $\text{Cu}_3\text{Pd}$ ,  $\text{O}^*$  is added to the surface via  $\text{O}_2$  adsorption and direct dissociation to  $2\text{O}^*$ . The first C–H bond of the *n*-butane molecule is activated via an  $\text{O}^*$ -assisted route, forming  $\text{C}_4\text{H}_9^*$  and  $\text{OH}^*$ .  $\text{C}_4\text{H}_9^*$  reacts with  $\text{O}^*$  to form



$C_4H_9O^*$ , and  $C_4H_9O^*$  reacts with  $OH^*$  to form  $C_4H_9OH^*$ . At the lower  $O_2$  pressure,  $O^*$  is added to the surface via  $H_2O$ -assisted dissociation. Since the  $O^*$  coverage is lower, the rate of rxn r1, i.e., direct C–H bond activation, is faster than the rate of rxn r3, i.e.,  $O^*$ -assisted C–H bond activation, and thus activation of  $C_4H_{10}^*$  produces  $C_4H_9^*$  and  $H^*$ . The  $C_4H_9^*$  that is formed then reacts with  $O^*$  to form  $C_4H_9O^*$ , which reacts with  $OH^*$  to form  $C_4H_9OH^*$ , as in the higher  $O_2$  pressure case. However, in this case,  $C_4H_9^*$  also reacts with  $OH^*$  and  $H_2O^*$ , reverting to  $n$ -butane, at approximately the same rate as it reacts with  $O^*$  to form  $C_4H_9O^*$ . Under this lower  $O_2$  pressure condition,  $OH^*$  is primarily formed via  $C_4H_9^*$  reaction with  $H_2O^*$ .

At the higher  $O_2$  pressure on  $Ag_3Pd$ ,  $O^*$  is added to the surface via  $O_2$  adsorption and direct dissociation to  $2O^*$ . The first C–H bond of  $C_4H_{10}^*$  is activated by both  $O^*$  and  $OH^*$ , forming  $C_4H_9^*$ . The dominant pathways for  $C_4H_9^*$  are the reaction with  $H^*$  to revert to  $C_4H_{10}^*$ , the reaction with  $O^*$  to form either  $C_4H_8O^*$  or  $C_4H_9O^*$ , and, most dramatically, the reaction with  $OH^*$  to form  $C_4H_8^*$ . The rate of the last of these is an order of magnitude greater than the rest, and indeed,  $C_4H_8(g)$  is the primary product from the  $Ag_3Pd$  surface. The  $C_4H_9O^*$  that does form from  $C_4H_9^*$  and  $O^*$  can react with  $O^*$  or with the  $Ag_3Pd$  surface itself to form  $C_4H_8O^*$ , and indeed, 1-butanol is the secondary product from the  $Ag_3Pd$  surface at 2 kPa  $O_2$ . At the lower  $O_2$  pressure,  $O^*$  intermediates do not participate in the dominant reaction pathway on  $Ag_3Pd$ . The  $n$ -butane molecule is activated directly by the catalyst surface, forming  $C_4H_9^*$ . This  $C_4H_9^*$  intermediate then reacts in part with  $H_2O^*$ , reverting back to  $C_4H_{10}^*$  and producing  $OH^*$ . The remaining  $C_4H_9^*$  reacts with this  $OH^*$ , forming  $C_4H_8^*$  and  $H_2O^*$ .

## 4. DISCUSSION

**4.1. How Catalytic Properties Influence Catalytic Activity and Selectivity.** Catalytic activity for production of 1-butanol, 1-butene, and 1-butanol on any given catalyst is highly sensitive to the formation energy of  $OH^*$  on that catalyst, with the activity for all three products decreasing significantly as the formation energy of  $OH^*$  decreases, i.e., becomes more negative, from the optimal values. According to the scaling relationship presented in Figure 2, the  $O^*$  formation energy increases with the  $OH^*$  formation energy; hence, surfaces with strong affinities for  $OH^*$  generate high coverages of  $O^*$ , which block catalytic sites needed for  $n$ -butane conversion. Accordingly,  $O^*$  is identified as a rate-inhibiting species in DRC analysis on  $Cu_3Pd$  at both  $O_2$  pressures and on  $Ag_3Pd$  at the higher  $O_2$  pressure (see Table 3, presented later in this paper).

The formation energy of  $OH^*$  also has a strong influence on catalytic selectivity for 1-butanol, with surfaces that bind  $OH^*$  too weakly favoring dehydrogenation instead of oxidation. This is demonstrated by analyzing the dominant reaction pathways on  $Ag_3Pd$ .  $Ag_3Pd$  has the weakest (most positive)  $OH^*$  formation energy, and thus also the weakest  $O^*$  formation energy, of the metals that we explicitly studied in this work. Since  $Ag_3Pd$  has a low affinity for  $OH^*$  and  $O^*$ , it is driven to convert these species. It is convenient to convert these species to  $H_2O^*$ , which has a consistently favorable (negative) formation energy on all of the transition-metal surfaces explicitly studied in this work. This promotes dehydrogenation of  $C_4^*$  species, since the H atoms that are needed to convert  $OH^*$  and  $O^*$  to  $H_2O^*$  are abstracted from the  $C_4^*$  species. Specifically, on  $Ag_3Pd$ ,  $O^*$  is converted to  $OH^*$  via dehydrogenation of  $C_4H_{10}^*$  and  $C_4H_9O^*$  to  $C_4H_9^*$  and  $C_4H_8O^*$ , respectively, and  $OH^*$  is converted to  $H_2O^*$  via  $C_4H_9^*$  dehydrogenation to  $C_4H_8^*$ . On the other hand,  $Cu_3Pd$  has a

stronger affinity for  $OH^*$  and, thus,  $O^*$ . At the lower  $O_2$  pressure, it readily oxidizes  $C_4H_9^*$  to  $C_4H_9O^*$ . At the higher  $O_2$  pressure, however, the affinity of  $Cu_3Pd$  for  $O^*$  is inhibiting, as a large coverage of  $O^*$  develops, which blocks surface sites for  $n$ -butane conversion.

Selectivity to 1-butanol is also sensitive to the formation energy of  $C^*$ . Figure 4 plots the rate of 1-butanol formation, with

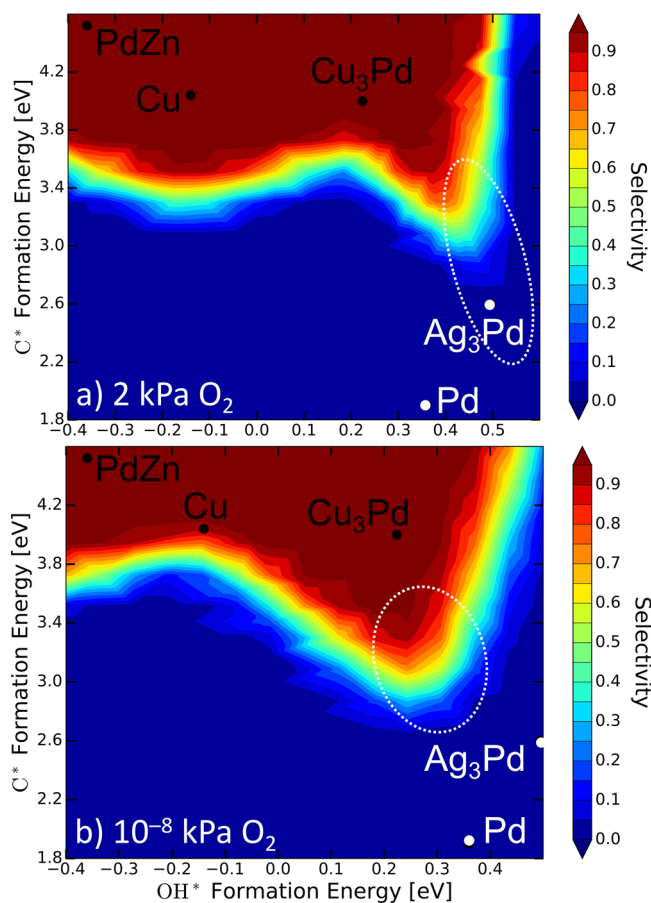


**Figure 4.** Heat maps showing the selectivity toward 1-butanol (i.e.,  $r_{1\text{-butanol}}/r_{n\text{-butane}}$ ), calculated as a continuous function of the descriptors at 423 K, 3750 kPa  $C_4H_{10}(g)$ , 456 kPa  $H_2O(g)$ , and (a) 2 kPa  $O_2(g)$  or (b)  $10^{-8}$  kPa  $O_2(g)$ . The dotted lines encompass descriptor values where  $r_{1\text{-butanol}} > 10^{-5}$  (in units of molecules per site per second). [1 eV = 96.485 kJ/mol.]

respect to the rate of  $n$ -butane adsorption (i.e.,  $r_{1\text{-butanol}}/r_{n\text{-butane}}$ ), as a function of the descriptors. There is a clear divide (separating the dark red regions from the dark blue regions in Figure 4) in the selectivity toward 1-butanol in the range of  $C^*$  formation energies from 3.0 eV to 3.5 eV over a wide range of values of the  $OH^*$  formation energy. Below this divide, catalysts favor C–H bond activation and, thus, products of overdehydrogenation, such as 1-butanol and 1-butene. Above the divide, catalysts are selective for 1-butanol. We find that the activation barriers for reactions involving dehydrogenation of  $C_4^*$  species are significantly correlated to the formation energy of  $C^*$  (see section S8 in the Supporting Information); therefore, when the formation energy of  $C^*$  is lower (more negative), the activation barriers for reactions involving C–H bond breaking are also lower. Catalysts with  $C^*$  formation energies below the “red/blue divide” illustrated in Figure 4 promote C–H bond activation readily and are thus not selective for 1-butanol.



Finally, the dotted lines in Figure 4 encompass descriptor values where the rate of 1-butanol desorption (calculated in microkinetic modeling) exceeds  $10^{-5}$  molecules per site per second, which is on the high end for the  $r_{1\text{-butanol}}$  calculated in this work. To achieve selectivity for 1-butanol near 1 and relatively high activity for 1-butanol, a catalyst must exhibit descriptor values in the red regions in Figure 4 that are also encompassed within the dotted lines. There is only a small window of descriptor values that achieve both high selectivity and relatively high activity. The greatest opportunity is at the lower  $O_2$  pressure of  $10^{-8}$  kPa, where descriptor values of 0.23 eV (formation energy of  $OH^*$ ) and 3.5 eV (formation energy of  $C^*$ ) are predicted to yield a selectivity of  $\sim 1$  and a rate just greater than  $10^{-5}$  molecules per site per second.

**4.2. Degree of Rate Control Analysis.** Calculated DRC values for the production of 1-butanol on  $Cu_3Pd$  at 423 K, 3750 kPa  $C_4H_{10}(g)$ , 456 kPa  $H_2O(g)$ , and  $10^{-8}$  kPa  $O_2$  and on  $Ag_3Pd$  at 423 K, 3750 kPa  $C_4H_{10}(g)$ , 456 kPa  $H_2O(g)$ , and 2 kPa  $O_2$  are presented in Table 3. These catalysts and conditions were chosen

**Table 3. Degrees of Rate Control in the Production of 1-Butanol (OH) or 1-Butanal (AL) Calculated from Microkinetic Modeling Data Obtained at 423 K, 3750 kPa  $C_4H_{10}(g)$ , 456 kPa  $H_2O(g)$ , and  $O_2(g)$  Pressures as Indicated for Select Catalytic Species**

	Degree of Rate Control		
	$Cu_3Pd:X_{OH_j}$ at $10^{-8}$ kPa $O_2$	$Ag_3Pd:X_{OH_j}$ at 2 kPa $O_2$	$Ag_3Pd:X_{AL_j}$ at 2 kPa $O_2$
$O^*$	−0.59	−2.5	−2.5
$H^*$	0.56		
$C_4H_8^*$			−0.56
transition state of $C_4H_{10}^* + O^* \leftrightarrow C_4H_9^* + OH^*$		2.0	2.0
transition state of $C_4H_9^* + O^* \leftrightarrow C_4H_9O^* + ^*$	0.60	0.87	0.87
transition state of $C_4H_9^* + OH^* \leftrightarrow C_4H_8^* + H_2O^*$			−0.24
transition state of $C_4H_9O^* + OH^* \leftrightarrow C_4H_9OH^* + O^*$		0.93	
transition state of $C_4H_9O^* + O^* \leftrightarrow C_4H_8O^* + OH^*$		−0.41	
transition state of $O_2^* + ^* \leftrightarrow 2O^*$		−1.1	−1.1

because they yield the highest activities for production of 1-butanol explicitly calculated in this work. Since the primary product of oxidation on  $Ag_3Pd$  at 423 K, 3750 kPa  $C_4H_{10}(g)$ , 456 kPa  $H_2O(g)$ , and 2 kPa  $O_2(g)$  is 1-butanol, the DRC values for the production of 1-butanol are also presented in Table 3. We note that we have only included DRC values  $>0.1$  in Table 3; however, the interested reader can find all the DRC values that we calculated in the Supporting Information (Table S7.1). Consistent with the discussion above,  $O^*$  is a rate-inhibiting species in all three cases; however, it has a much less significant effect on the rate on  $Cu_3Pd$ . The rate-controlling step on  $Cu_3Pd$  is  $C_4H_9^* + O^* \leftrightarrow C_4H_9O^* + ^*$ , which indicates that if the activation barrier for this step were decreased, the rate of 1-butanol desorption would increase.

On  $Ag_3Pd$  at 2 kPa  $O_2$ ,  $n$ -butane activation and 1-butyl oxidation to 1-butoxy are rate-controlling in the pathways toward catalytic oxidation. Furthermore, the DRC value for 1-butyl dehydrogenation, i.e.,  $C_4H_9^* + OH^* \leftrightarrow C_4H_8^* + H_2O^*$ , is negative in the production of 1-butanol. Therefore, 1-butyl represents a branch point in the pathway of catalytic

dehydrogenation versus catalytic oxidation: If the barrier of  $C_4H_9^* + OH^* \leftrightarrow C_4H_8^* + H_2O^*$  were higher or the barrier of  $C_4H_9^* + O^* \leftrightarrow C_4H_9O^* + ^*$  were lower, the rate of 1-butanol desorption would increase, i.e., catalytic oxidation would become more favorable, with respect to catalytic dehydrogenation. Similarly, the DRC value for molecular oxygen dissociation is negative for the desorption rates of 1-butanol and 1-butanol, since this reaction maintains the coverage of  $O^*$ , which, as discussed above, promotes dehydrogenation of the  $C_4^*$  species. Finally, the transition state for  $C_4H_9O^* + OH^* \leftrightarrow C_4H_9OH^* + O^*$  has a positive DRC value in the production of 1-butanol, whereas the transition state for  $C_4H_9O^* + O^* \leftrightarrow C_4H_8O^* + OH^*$  has a negative DRC value. Therefore, 1-butoxy represents a branch point in the pathway toward 1-butanol versus 1-butanol. The barrier of  $C_4H_9O^* + OH^* \leftrightarrow C_4H_9OH^* + O^*$  would need to be lower, or the barrier of  $C_4H_9O^* + O^* \leftrightarrow C_4H_8O^* + OH^*$  would need to be higher, in order for  $Ag_3Pd$  to become more favorable toward 1-butanol production instead of 1-butanol production.

## 5. CONCLUSIONS

In summary, we have used a combination of DFT calculations and microkinetic modeling to study reactions of  $n$ -butane over sterically constrained metal (111) surfaces, for the purpose of identifying catalyst characteristics that lead to the active and selective production of 1-butanol. We determined that achieving high activity and selectivity requires very precise tuning of the catalytic properties. Specifically, catalytic affinity for  $OH^*$  and  $O^*$  is key: catalysts that bind  $O^*$  too strongly develop coverages of  $O^*$  that are too high, and the  $O^*$  adsorbates block catalytic sites and inhibit the rate of  $n$ -butane conversion. Conversely, catalysts that bind  $O^*$  and  $OH^*$  too weakly promote catalytic dehydrogenation of  $C_4^*$  species, as this process supplies H atoms that convert  $O^*$  and  $OH^*$  to  $H_2O^*$ , which is generally stable on the transition-metal surfaces examined in this work. Furthermore, a catalyst's affinity for  $C^*$  helps to determine its selectivity, since the formation energy of  $C^*$  on the catalyst surface is correlated to the catalyst's ability to activate C–H bonds. Because of this correlation, catalysts that bind  $C^*$  too strongly prefer catalytic dehydrogenation instead of catalytic oxidation and are thus not selective for 1-butanol. There is a very small window where it is possible to achieve high selectivity and activity for 1-butanol, which very finely balances catalytic affinity for  $C^*$  and  $OH^*$ . The reaction  $C_4H_9^* + O^* \leftrightarrow C_4H_9O^* + ^*$  is a rate-controlling step on the most active catalysts studied in this work; therefore, catalysts that promote this reaction readily should have potential as active catalysts for  $n$ -butane oxidation to 1-butanol.

## ■ ASSOCIATED CONTENT

### Supporting Information

The Supporting Information is available free of charge on the ACS Publications website at DOI: 10.1021/acs.iecr.8b00589.

Structures of reaction intermediates and transition states; CatMAP input file details; conversion between formation energies and electronic energies; table of reaction energies and activation barriers for all reaction steps on all surfaces; scaling relationships for all intermediates and transition states; table of mean absolute error and root-mean-square deviation for different descriptor sets; table of degree of rate control values for all species on the  $Cu_3Pd$ , Pd, and  $Ag_3Pd$  surfaces; VASP CONTCARs for all reaction

intermediates and all transition states on all surfaces  
(PDF)

## AUTHOR INFORMATION

### Corresponding Author

\*E-mail: [rgetman@clemson.edu](mailto:rgetman@clemson.edu).

### ORCID

Rachel B. Getman: 0000-0003-0755-0534

### Notes

The authors declare no competing financial interest.

### Biographies



**Jiazhou Zhu** received his B.S. degrees in Chemical Engineering from East China University of Science and Technology and University of Missouri-Columbia. He is currently a Ph.D. candidate in Chemical Engineering at Clemson University, under the supervision of Prof. Rachel Getman. His research interests include design of MOF encapsulated materials and computational screening using machine learning algorithms.



**Rachel B. Getman** earned her Ph.D. in Chemical Engineering from the University of Notre Dame in 2009. After postdoctoral research at Northwestern University, she joined the faculty at Clemson University in 2011. She is presently an Associate Professor in the Department of Chemical and Biomolecular Engineering and is notably the first woman to receive tenure and promotion to Associate Professor in chemical engineering at Clemson University. Dr. Getman serves on the executive boards of the Southeastern Catalysis Society and the Catalysis and Reaction Engineering Division of the American Institute of Chemical Engineers. Her research interests include using molecular simulations and multiscale modeling to elucidate materials function in order to facilitate materials design.

## ACKNOWLEDGMENTS

This research was funded by the National Science Foundation, under Award No. DMR-1334928. Simulations were performed on the Palmetto Supercomputer Cluster, which is maintained by the Cyberinfrastructure Technology Integration Group at Clemson University. We thank Dr. Steven Pellizzeri for technical assistance with the CatMAP software and for helpful discussions.

## REFERENCES

- (1) Periana, R. A.; Bhalla, G.; Tenn, W. J.; Young, K. J.; Liu, X. Y.; Mironov, O.; Jones, C.; Ziatdinov, V. R. Perspectives on some challenges and approaches for developing the next generation of selective, low temperature, oxidation catalysts for alkane hydroxylation based on the CH activation reaction. *J. Mol. Catal. A: Chem.* **2004**, 220 (1), 7–25.
- (2) Brazdil, J. F. Strategies for the selective catalytic oxidation of alkanes. *Top. Catal.* **2006**, 38 (4), 289–294.
- (3) Zvaigzne, A. I.; Teng, I.; Martinez, E.; Trejo, J.; Acree, W. E. Solubility of anthracene in binary alkane + 1-propanol and alkane + 1-butanol solvent mixtures. *J. Chem. Eng. Data* **1993**, 38 (3), 389–392.
- (4) Pasquini, D.; Pimenta, M. T.; Ferreira, L. H.; Curvelo, A. A. Sugar cane bagasse pulping using supercritical CO<sub>2</sub> associated with co-solvent 1-butanol/water. *J. Supercrit. Fluids* **2005**, 34 (2), 125–131.
- (5) Wang, H.; Nakamura, H.; Yao, K.; Maeda, H.; Abe, E. Effect of solvents on the preparation of silica-coated magnetic particles. *Chem. Lett.* **2001**, 30 (11), 1168–1169.
- (6) Uhde, E.; Salthammer, T. Impact of reaction products from building materials and furnishings on indoor air quality—A review of recent advances in indoor chemistry. *Atmos. Environ.* **2007**, 41 (15), 3111–3128.
- (7) Labinger, J. A.; Bercaw, J. E. Understanding and exploiting C–H bond activation. *Nature* **2002**, 417 (6888), 507–514.
- (8) Labinger, J. A. Selective alkane oxidation: Hot and cold approaches to a hot problem. *J. Mol. Catal. A: Chem.* **2004**, 220 (1), 27–35.
- (9) Stephenson, C. J.; Hupp, J. T.; Farha, O. K. Pt@ ZIF-8 composite for the regioselective hydrogenation of terminal unsaturations in 1,3-dienes and alkynes. *Inorg. Chem. Front.* **2015**, 2 (5), 448–452.
- (10) Lu, G.; Li, S.; Guo, Z.; Farha, O. K.; Hauser, B. G.; Qi, X.; Wang, Y.; Wang, X.; Han, S.; Liu, X.; et al. Imparting functionality to a metal–organic framework material by controlled nanoparticle encapsulation. *Nat. Chem.* **2012**, 4 (4), 310–316.
- (11) Zhang, M.; Yang, Y.; Li, C.; Liu, Q.; Williams, C. T.; Liang, C. PVP–Pd@ ZIF-8 as highly efficient and stable catalysts for selective hydrogenation of 1,4-butanediol. *Catal. Sci. Technol.* **2014**, 4 (2), 329–332.
- (12) Li, H.; Eddaoudi, M.; O’Keeffe, M.; Yaghi, O. M. Design and synthesis of an exceptionally stable and highly porous metal–organic framework. *Nature* **1999**, 402 (6759), 276–279.
- (13) Chen, Z.-X.; Neyman, K. M.; Lim, K. H.; Rösch, N. CH<sub>3</sub>O decomposition on PdZn(111), Pd(111), and Cu(111). A theoretical study. *Langmuir* **2004**, 20 (19), 8068–8077.
- (14) Lim, K. H.; Chen, Z.-X.; Neyman, K. M.; Rösch, N. Comparative theoretical study of formaldehyde decomposition on PdZn, Cu, and Pd surfaces. *J. Phys. Chem. B* **2006**, 110 (30), 14890–14897.
- (15) Chin, Y.-H.; Iglesia, E. Elementary steps, the role of chemisorbed oxygen, and the effects of cluster size in catalytic CH<sub>4</sub>–O<sub>2</sub> reactions on palladium. *J. Phys. Chem. C* **2011**, 115 (36), 17845–17855.
- (16) Dix, S. T.; Gómez-Gualdrón, D. A.; Getman, R. B. Implications of sterically constrained *n*-butane oxidation reactions on the reaction mechanism and selectivity to 1-butanol. *Surf. Sci.* **2016**, 653, 11–21.
- (17) Chin, Y.-H.; Buda, C.; Neurock, M.; Iglesia, E. Selectivity of chemisorbed oxygen in C–H bond activation and CO oxidation and kinetic consequences for CH<sub>4</sub>–O<sub>2</sub> catalysis on Pt and Rh clusters. *J. Catal.* **2011**, 283 (1), 10–24.
- (18) Chin, Y.-H.; Buda, C.; Neurock, M.; Iglesia, E. Consequences of metal–oxide interconversion for C–H bond activation during CH<sub>4</sub> reactions on Pd catalysts. *J. Am. Chem. Soc.* **2013**, 135 (41), 15425–15442.

- (19) Chin, Y.-H.; Buda, C.; Neurock, M.; Iglesia, E. Reactivity of chemisorbed oxygen atoms and their catalytic consequences during  $\text{CH}_4$ - $\text{O}_2$  catalysis on supported Pt clusters. *J. Am. Chem. Soc.* **2011**, *133* (40), 15958–15978.
- (20) Zuo, Z.-J.; Wang, L.; Han, P.-D.; Huang, W. Insights into the reaction mechanisms of methanol decomposition, methanol oxidation and steam reforming of methanol on Cu (111): A density functional theory study. *Int. J. Hydrogen Energy* **2014**, *39* (4), 1664–1679.
- (21) Lin, S.; Xie, D.; Guo, H. Pathways of methanol steam reforming on PdZn and comparison with Cu. *J. Phys. Chem. C* **2011**, *115* (42), 20583–20589.
- (22) Xing, B.; Pang, X.-Y.; Wang, G.-C. C–H bond activation of methane on clean and oxygen pre-covered metals: A systematic theoretical study. *J. Catal.* **2011**, *282* (1), 74–82.
- (23) Verma, P.; Vogiatzis, K. D.; Planas, N.; Borycz, J.; Xiao, D. J.; Long, J. R.; Gagliardi, L.; Truhlar, D. G. Mechanism of Oxidation of Ethane to Ethanol at Iron(IV)–Oxo Sites in Magnesium-Diluted  $\text{Fe}_2$  (dobdc). *J. Am. Chem. Soc.* **2015**, *137* (17), 5770–5781.
- (24) Meinhold, P.; Peters, M. W.; Chen, M. M.; Takahashi, K.; Arnold, F. H. Direct conversion of ethane to ethanol by engineered cytochrome P450 BM3. *ChemBioChem* **2005**, *6* (10), 1765–1768.
- (25) Xiao, D. J.; Bloch, E. D.; Mason, J. A.; Queen, W. L.; Hudson, M. R.; Planas, N.; Borycz, J.; Dzubak, A. L.; Verma, P.; Lee, K.; et al. Oxidation of ethane to ethanol by  $\text{N}_2\text{O}$  in a metal–organic framework with coordinatively unsaturated iron(II) sites. *Nat. Chem.* **2014**, *6* (7), 590–595.
- (26) Gesser, H.; Hunter, N.; Das, P. The ozone sensitized oxidative conversion of methane to methanol and ethane to ethanol. *Catal. Lett.* **1992**, *16* (1), 217–221.
- (27) Yoon, Y. S.; Ueda, W.; Moro-oka, Y. Oxidative dehydrogenation of propane over magnesium molybdate catalysts. *Catal. Lett.* **1995**, *35* (1–2), 57–64.
- (28) Bettahar, M.; Costentin, G.; Savary, L.; Lavalley, J. On the partial oxidation of propane and propylene on mixed metal oxide catalysts. *Appl. Catal., A* **1996**, *145* (1–2), 1–48.
- (29) Grabow, L. C. In *Computational Catalysis*; Asthagiri, A., Janik, M. J., Eds.; Royal Society of Chemistry: London, 2013.
- (30) Dix, S. T.; Scott, J. K.; Getman, R. B.; Campbell, C. T. Using degrees of rate control to improve selective *n*-butane oxidation over model MOF-encapsulated catalysts: Sterically-constrained  $\text{Ag}_3\text{Pd}(111)$ . *Faraday Discuss.* **2016**, *188*, 21–38.
- (31) Gómez-Gualdrón, D. A.; Dix, S. T.; Getman, R. B.; Snurr, R. Q. A modelling approach for MOF-encapsulated metal catalysts and application to *n*-butane oxidation. *Phys. Chem. Chem. Phys.* **2015**, *17* (41), 27596–27608.
- (32) Davey, W. P. Precision measurements of the lattice constants of twelve common metals. *Phys. Rev.* **1925**, *25* (6), 753.
- (33) Rayne, J. Elastic constants of palladium from 4.2–300° K. *Phys. Rev.* **1960**, *118* (6), 1545.
- (34) Kresse, G.; Furthmüller, J. Efficiency of ab-initio total energy calculations for metals and semiconductors using a plane-wave basis set. *Comput. Mater. Sci.* **1996**, *6* (1), 15–50.
- (35) Kresse, G.; Furthmüller, J. Efficient iterative schemes for ab initio total-energy calculations using a plane-wave basis set. *Phys. Rev. B: Condens. Matter Mater. Phys.* **1996**, *54* (16), 11169.
- (36) Perdew, J. P.; Burke, K.; Ernzerhof, M. Generalized gradient approximation made simple. *Phys. Rev. Lett.* **1996**, *77* (18), 3865.
- (37) Blöchl, P. E. Projector augmented-wave method. *Phys. Rev. B: Condens. Matter Mater. Phys.* **1994**, *50* (24), 17953.
- (38) Grimme, S. Semiempirical GGA-type density functional constructed with a long-range dispersion correction. *J. Comput. Chem.* **2006**, *27* (15), 1787–1799.
- (39) Henkelman, G.; Jónsson, H. Improved tangent estimate in the nudged elastic band method for finding minimum energy paths and saddle points. *J. Chem. Phys.* **2000**, *113* (22), 9978–9985.
- (40) Henkelman, G.; Uberuaga, B. P.; Jónsson, H. A climbing image nudged elastic band method for finding saddle points and minimum energy paths. *J. Chem. Phys.* **2000**, *113* (22), 9901–9904.
- (41) Henkelman, G.; Jónsson, H. A dimer method for finding saddle points on high dimensional potential surfaces using only first derivatives. *J. Chem. Phys.* **1999**, *111* (15), 7010–7022.
- (42) Breslin, T.; Edén, P.; Krogh, M. Comparing functional annotation analyses with Catmap. *BMC Bioinf.* **2004**, *5* (1), 193.
- (43) Pellizzeri, S.; Jones, I. A.; Doan, H. A.; Snurr, R. Q.; Getman, R. B. Using Gas-Phase Clusters to Screen Porphyrin-Supported Nanocluster Catalysts for Ethane Oxidation to Ethanol. *Catal. Lett.* **2016**, *146* (12), 2566–2573.
- (44) Jalid, F.; Khan, T. S.; Mir, F. Q.; Haider, M. A. Understanding trends in hydrodeoxygenation reactivity of metal and bimetallic alloy catalysts from ethanol reaction on stepped surface. *J. Catal.* **2017**, *353*, 265–273.
- (45) Baek, B.; Aboiralar, A.; Wang, S.; Kharidehal, P.; Grabow, L. C.; Massa, J. D. Strategy to improve catalytic trend predictions for methane oxidation and reforming. *AIChE J.* **2017**, *63* (1), 66–77.
- (46) Stegelmann, C.; Andreasen, A.; Campbell, C. T. Degree of rate control: How much the energies of intermediates and transition states control rates. *J. Am. Chem. Soc.* **2009**, *131* (23), 8077–8082.
- (47) Campbell, C. T. Finding the rate-determining step in a mechanism: comparing dedonder relations with the “Degree of Rate Control”. *J. Catal.* **2001**, *204* (2), 520–524.
- (48) Wolcott, C. A.; Medford, A. J.; Studt, F.; Campbell, C. T. Degree of rate control approach to computational catalyst screening. *J. Catal.* **2015**, *330*, 197–207.
- (49) Hibbitts, D.; Neurock, M. Promotional effects of chemisorbed oxygen and hydroxide in the activation of C–H and O–H bonds over transition metal surfaces. *Surf. Sci.* **2016**, *650*, 210–220.
- (50) Gao, Y.; Zeng, X. C. Water-promoted  $\text{O}_2$  dissociation on small-sized anionic gold clusters. *ACS Catal.* **2012**, *2* (12), 2614–2621.
- (51) Chang, C.-R.; Yang, X.-F.; Long, B.; Li, J. A water-promoted mechanism of alcohol oxidation on a Au(111) surface: Understanding the catalytic behavior of bulk gold. *ACS Catal.* **2013**, *3* (8), 1693–1699.